Supplementary Information (SI) for Energy & Environmental Science.
This journal is © The Royal Society of Chemistry 2024

Supporting Information

Rationally coupling thermal tolerance, thermal conductance, and overheating-response in a separator for safe batteries

Haotian Lu[1,2,3,4#], Ao Du[1,3#], Xiaoping Lin[5], Ziyi Zhang[1,3], Sisi Liu[1,3], Yuansen Xie[5], Wenhao Li[6], Jianwei Song[6], Yuhao Lu[5], Wei Chen[2,4,7], Chunpeng Yang[1,3*], and Quan-Hong Yang[1,2,3*]

[1]Nanoyang Group, Tianjin Key Laboratory of Advanced Carbon and Electrochemical Energy Storage, School of Chemical Engineering and Technology, National Industry-Education Integration Platform of Energy Storage, Tianjin University, Tianjin 300072, China.

[2]Joint School of National University of Singapore and Tianjin University, International Campus of Tianjin University, Fuzhou 350207, China.

[3]Haihe Laboratory of Sustainable Chemical Transformations, Tianjin 300192, China.

[4]Department of Chemistry, National University of Singapore, 117543, Singapore.

[5]Key Laboratory of Consumer Lithium-Ion Battery in Fujian, Ningde Amperex Technology Ltd (ATL), Ningde 352100, China.

[6]State Key Laboratory for Strength and Vibration of Mechanical Structures, Xi'an Jiaotong University, Xi'an 710049, China.

[7]Department of Physics, National University of Singapore, 117542, Singapore.

[#]H.L. and A.D. contributed equally to this work.

[*]E-mail: cpyang@tju.edu.cn, qhyangcn@tju.edu.cn

The detail information of simulation methods. We performed finite element method (FEM) to investigate the effects of separator characteristics on the thermal management of Li-based batteries, by using the electro-chemo-thermal coupling model. The geometry for the pouch cell consists of multilayered Al collector/cathode/separator/anode/Cu collector units and Al-plastic films, as shown in Supplementary Fig. 23. Galvanostatic discharging occurs at a 1C rate. The cathode domain consists of NCM811 active particles, carbon, binder, and electrolyte. The separator domain consists of a separator matrix and electrolyte. For Li anode, the anode domain is Li metal foil. For carbon anode, the anode domain consists of graphite active particles, carbon, binder, and electrolyte. (1) The pseudo-three-dimensional model is used to describe the mass and charge conservations in the cathode, anode, and separator domains. (a) In the cathode and carbon anode domains, the Li-ion transport process in the electrolyte phase is described by:

$$\varepsilon_{\mathrm{e}} \frac{\partial c_{\mathrm{Li}^+}}{\partial t} = \nabla \left(D_{\mathrm{l}}^{\mathrm{eff}} \nabla c_{\mathrm{Li}^+} \right) + a(1-t_+) j$$

where ε_{e} is the porosity of the electrode, c_{Li^+} is the concentration of Li-ion, t is time, $D_{\mathrm{l}}^{\mathrm{eff}}$ is the diffusion coefficient of Li-ion in the electrolyte phase, a is the specific surface area of active material, t_+ is the transference number of Li-ion, and j is the local current density of the Faradic reaction. The Li transport process in the NCM811 and graphite active particles is described by:

$$\frac{\partial c_{\mathrm{s}}}{\partial t} = \frac{\partial D_{\mathrm{s}}}{r^2} \frac{\partial}{\partial t} \left(r^2 \frac{\partial c_{\mathrm{s}}}{\partial t} \right)$$

where c_{s} is the solid phase concentration of Li-atom, D_{s} is the diffusion coefficient of Li-atom in the solid phase, and r is the particle radius of active material. The charge conservation process in the electrolyte phase is described by:

$$i_{\mathrm{l}} = -\sigma_{\mathrm{l}}^{\mathrm{eff}} \nabla \varphi_{\mathrm{l}} + \frac{2\sigma_{\mathrm{l}}^{\mathrm{eff}} RT}{F}(1-t_{+})\nabla \ln c_{\mathrm{Li}^{+}}$$

where i_{l} is the current density of the electrolyte phase, $\sigma_{\mathrm{l}}^{\mathrm{eff}}$ is the electric conductivity of the electrolyte phase, φ_l is the electric potential of the electrolyte phase, and T is the working temperature. The charge conservation process in the solid phase including Li metal foil is described by:

$$i_{\mathrm{s}} = -\sigma_{\mathrm{s}}^{\mathrm{eff}} \nabla \varphi_{\mathrm{s}}$$

where i_{s} is the current density of the solid phase, $\sigma_{\mathrm{s}}^{\mathrm{eff}}$ is the electric conductivity of the solid phase, and φ_{s} is the electric potential of the solid phase. The Faradic reaction process in the cathode-electrolyte or carbon anode-electrolyte interface is described by:

$$j = Fk_r c_{\mathrm{s}}^{a_{\mathrm{c}}} (c_{\mathrm{s,max}} - c_{\mathrm{s}})^{a_{\mathrm{a}}} (\exp(\frac{a_{\mathrm{a}} F\eta}{RT}) - \exp(\frac{-a_{\mathrm{c}} F\eta}{RT}))$$

where k_r is the rate constant of the Faradic reaction, a_{c} is the cathode charge transfer coefficient, a_{a} is the anode charge transfer coefficient, $c_{\mathrm{s,max}}$ is the maximal solid concentration of Li-atom, and η is the over-potential of the Faradic reaction. The Faradic reaction process in the Li anode-electrolyte interface is described by:

$$j = i_0(\exp(\frac{a_{\mathrm{a}} F\eta}{RT}) - \exp(\frac{-a_{\mathrm{c}} F\eta}{RT}))$$

where i_0 is the exchange current density of Li deposition reaction.

(b) In the separator domain, the Li-ion transport process in the electrolyte phase is described by:

$$\varepsilon_{\mathrm{sp}} \frac{\partial c_{\mathrm{Li}^{+}}}{\partial t} = \nabla(D_{\mathrm{l,sp}}^{\mathrm{eff}} \nabla \mathrm{c}_{\mathrm{Li}^{+}})$$

where $\varepsilon_{\mathrm{sp}}$ is the porosity of the separator and $D_{\mathrm{l,sp}}^{\mathrm{eff}}$ is the diffusion coefficient of Li-ion in

the electrolyte phase. The charge conservation process in the electrolyte phase is described by:

$$i_{\mathrm{l}} = -\sigma_{\mathrm{l,sp}}^{\mathrm{eff}} \nabla \varphi_{\mathrm{l}} + \frac{2\sigma_{\mathrm{l,sp}}^{\mathrm{eff}} RT}{F}(1 - t_{+}) \nabla \ln c_{\mathrm{Li}^{+}}$$

where $\sigma_{\mathrm{l,sp}}^{\mathrm{eff}}$ is the electric conductivity of the electrolyte phase.

(2) The energy equation is used to describe the energy conservations in all domains including Al collector, Cu collector, and Al-plastic film. (a) In the cathode and carbon anode domains, the energy conservation phase is described by:

$$\rho c_{\mathrm{p}} \frac{\partial T}{\partial t} = \nabla (k_{\mathrm{c}} \nabla T) + Q_{\mathrm{j}} + Q_{\mathrm{r}}$$

$$Q_{\mathrm{j}} = -(i_{\mathrm{s}} \nabla \varphi_{\mathrm{s}} + i_{\mathrm{l}} \nabla \varphi_{\mathrm{l}})$$

$$Q_{\mathrm{r}} = aj(\varphi_{\mathrm{s}} - \varphi_{\mathrm{l}} - E_{\mathrm{eq}} + T \frac{\partial E_{\mathrm{eq}}}{\partial T})$$

(b) In the Li anode domain, the energy conservation phase is described by:

$$\rho c_{\mathrm{p}} \frac{\partial T}{\partial t} = \nabla (k_{\mathrm{c}} \nabla T) + Q_{\mathrm{j}}$$

$$Q_{\mathrm{j}} = -i_{\mathrm{s}} \nabla \varphi_{\mathrm{s}}$$

(c) At the interface of the anode and electrolyte, the energy conservation phase is described by:

$$Q_{\mathrm{r}} = aj(\varphi_{\mathrm{s}} - \varphi_{\mathrm{l}} - E_{\mathrm{eq}} + T \frac{\partial E_{\mathrm{eq}}}{\partial T})$$

(b) In the separator domain, the energy conservation phase is described by:

$$\rho c_{\mathrm{p}} \frac{\partial T}{\partial t} = \nabla (k_{\mathrm{c}} \nabla T) + Q_{\mathrm{j}}$$

$$Q_{\mathrm{j}} = -i_{\mathrm{l}} \nabla \varphi_{\mathrm{l}}$$

(c) In the Al and Cu collector domains, the energy conservation phase is described by:

$$\rho c_{\mathrm{p}} \frac{\partial T}{\partial t} = \nabla (k_{\mathrm{c}} \nabla T) + Q_{\mathrm{j}}$$

$$Q_{\mathrm{j}} = -i_{\mathrm{s}} \nabla \varphi_{\mathrm{s}}$$

(d) In the Al-plastic domains, the energy conservation phase is described by:

$$\rho c_{\mathrm{p}} \frac{\partial T}{\partial t} = \nabla (k_{\mathrm{c}} \nabla T)$$

where ρ is the material density, c_{p} is the specific heat of the material, k_{c} is the thermal conductivity of the material, Q_{j} is the generation rate of joule heat, Q_{r} is the generation rate of reaction heat, and E_{eq} is the balance potential of the Faradic reaction. The parameters mentioned above are detailed in Supplementary Tables 5 and 6.

We also conducted a FEM to investigate the effect of temperature distribution on the Li deposition morphology. The temperature distribution was preset to be consistent with the infrared thermal results by using a location-dependent function,

$$T = f(T_{\max}, T_{\min}, x, y)$$

where T is the local temperature, $T_{\max}$ is the highest temperature, $T_{\min}$ is the lowest temperature, x and y are location indexes. The temporal and spatial evolution of Li deposition morphology was simulated by coupling different temperature distributions, the phase-field model (Eq. 21), the Nernst-Plank equation (Eq. 22), and the Poisson equation (Eq. 23),

$$\frac{\partial \xi}{\partial t} = -L_\sigma (g^{'}(\xi) - \kappa \nabla^2 \xi) - L_\eta h^{'}(\xi) \left\{ \exp\left[\frac{(1-\alpha) F \eta}{RT} \right] - c_{\mathrm{Li}^+} \exp\left[\frac{-\alpha F \eta}{RT} \right] \right\}$$

$$\frac{\partial c_{\mathrm{Li}^+}}{\partial t} = \nabla \cdot (D_{\mathrm{Li}^+}^{\mathrm{eff}} \nabla c_{\mathrm{Li}^+} + \frac{D_{\mathrm{Li}^+}^{\mathrm{eff}} c_{\mathrm{Li}^+} F}{RT} \nabla \varphi) - c_{\mathrm{s}} \frac{\partial \xi}{\partial t}$$

$$\nabla \cdot (\sigma^{\mathrm{eff}} \nabla \varphi) = i_{\mathrm{R}}$$

where ξ is the phase-field parameter ($\xi = 0$ for the electrolyte and $\xi = 1$ for the Li metal), $g(\xi)$ is the arbitrary double well function, κ is the surface energy anisotropy, L_σ is the interface mobility, L_η is the reaction-related constant, $h(\xi)$ is an interpolating function, α is the charge-transfer coefficient, η is the reaction overpotential, c_{Li^+} is the local Li-ion concentration, F the Faraday's constant, $D_{\mathrm{Li}^+}^{\mathrm{eff}}$ is the effective diffusion coefficient of Li-ion, c_{s} is the site density of Li metal, σ^{eff} is the effective conductivity, i_{R} is the current density. The parameters mentioned above are detailed in the Supplementary Table 7. All FEM simulations were solved on COMSOL Multiphysics 6.0.

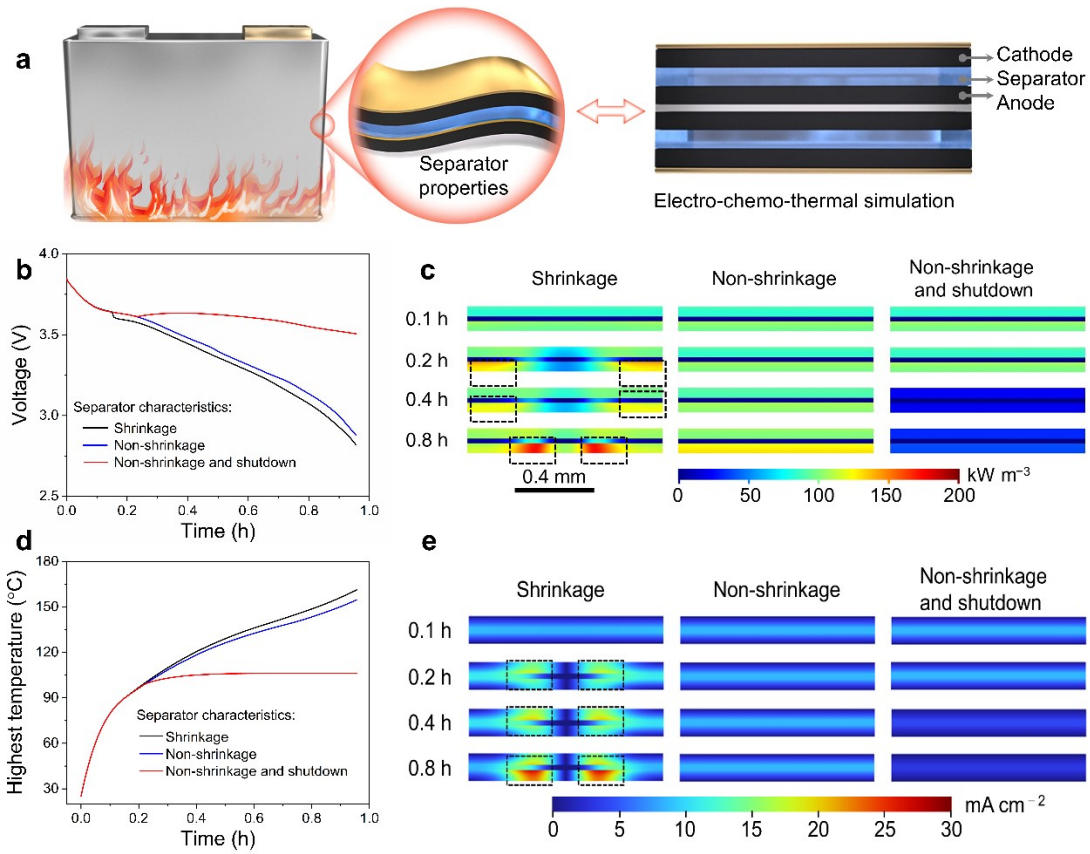

Supplementary Fig. 1 | Mitigation of cell thermal runaway by the thermal TCOR separator for NCM811|Carbon system. (a) Schematic illustration to simulate the effect of separator thermal properties on mitigating thermal runaway of the cell under thermal abuse conditions. (b) Simulation result of discharge voltage profiles of cells with different separator characteristics, including shrinkage, non-shrinkage, and non-shrinkage and shutdown in high-temperature environment (90 °C). (c) Simulation result of heat generation rate inside cells and (d) simulation result of the highest local temperature inside cells with different separator characteristics in high-temperature environment (90 °C). (e) Simulation results of current distribution inside the cells with different separator characteristics in high-temperature environment (90 °C).

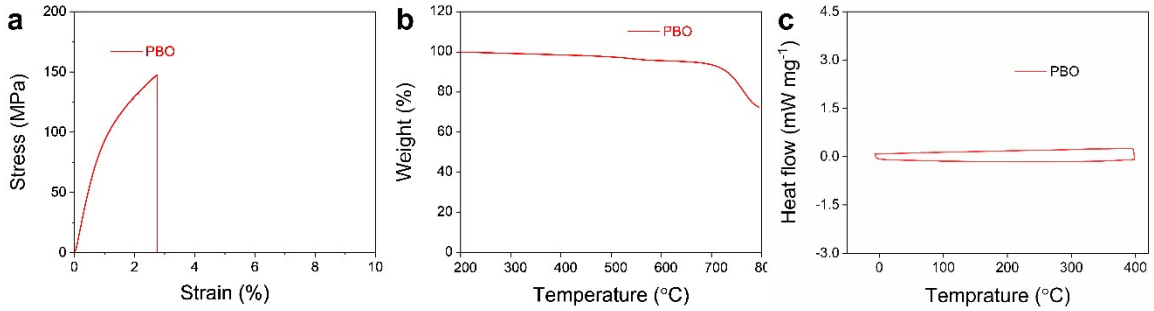

Supplementary Fig. 2 | The mechanical-thermal properties of PBO membrane. The PBO membrane has high tensile strength (147.22 MPa) and high Young's modulus (10.73 GPa), excellent thermal stability (670 °C) and superior thermal-tolerance property (no melting point). The DSC results of the PBO membranes show no discernible endothermic peak until 400 °C, indicating no observable phase change occurs in the PBO membranes.

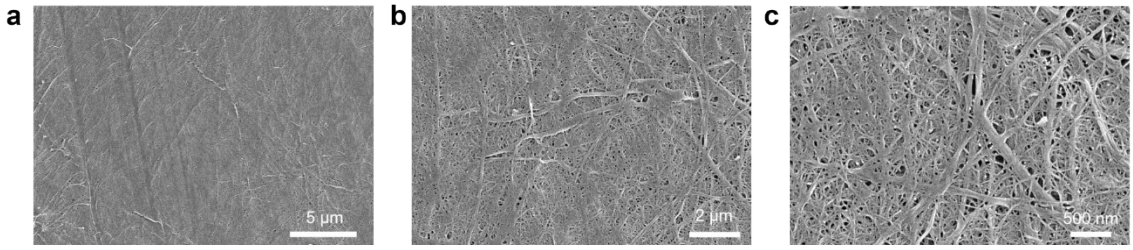

Supplementary Fig. 3 | Top-view SEM images of the PBO membrane. The SEM images show that the PBO membrane has flat surface to facilitate practical application and have porous structure to provide convenience for ion transport.

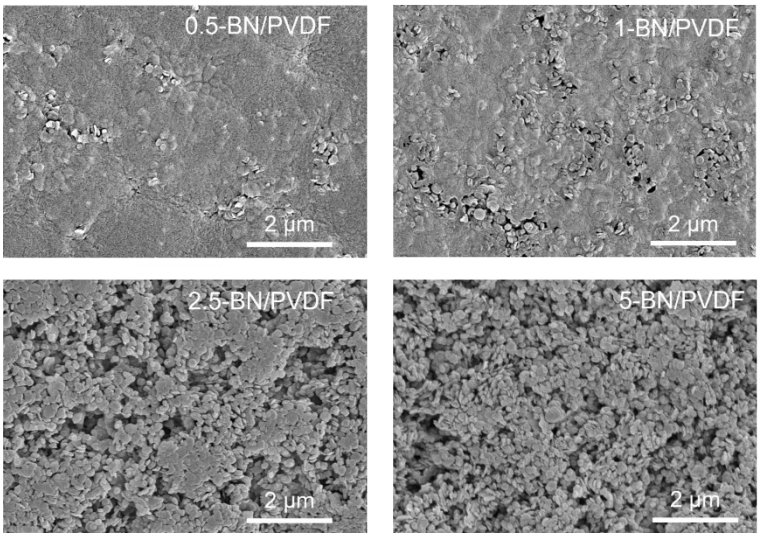

Supplementary Fig. 4 | Top-view SEM images of (**a**) 0.5-BN:PVDF, (**b**) 1-BN:PVDF, (**c**) 2.5-BN:PVDF, and (**d**) 5-BN:PVDF (*x*-BN/PVDF, where *x* is the mass ratio of BN and PVDF). The SEM images under different mass ratios of BN/PVDF show that the large amount of BN is conducive to porosity improvement. Meanwhile, we optimally selected the 2.5-BN/PVDF composite coating to ensure high porosity, high thermal conductivity, and overheating responsiveness.

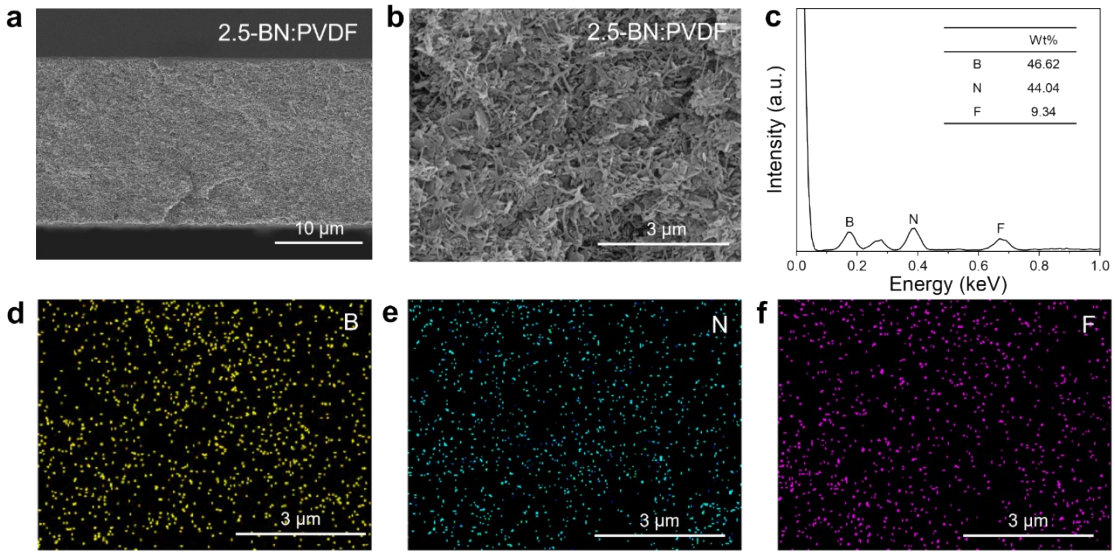

Supplementary Fig. 5 | (**a-b**) Cross-view SEM images of 2.5-BN:PVDF. (**c-f**) EDS mapping images of B, N, and F of 2.5-BN/PVDF. The cross-view SEM images reveal that BN nanosheets are uniformly dispersed in the PVDF matrix, and the EDS mapping images also shows the B and N elements are evenly dispersed within PVDF matrix. The above results indicate that BN nanosheets uniformly disperse with the PVDF matrix.

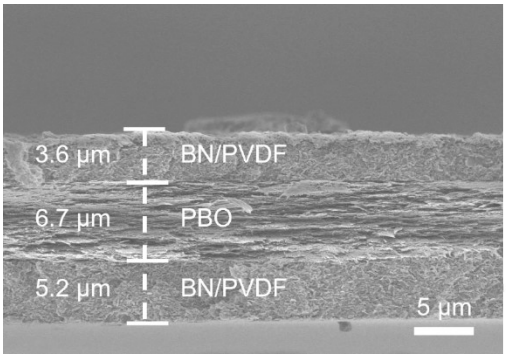

Supplementary Fig. 6 | Cross-view SEM image of PBO-BN/PVDF separator.

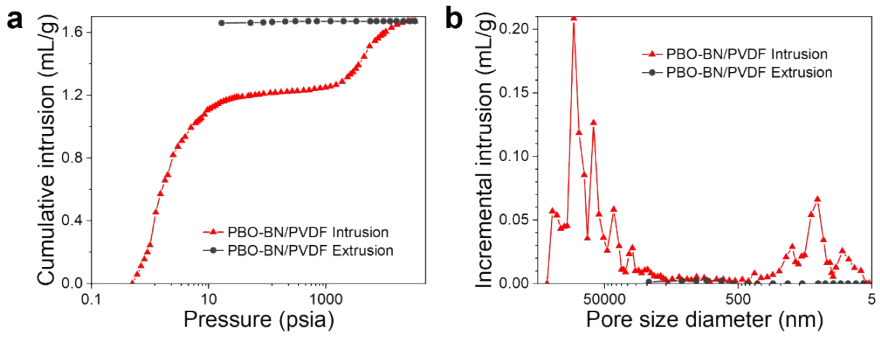

Supplementary Fig. 7 | Mercury intrusion porosimetry testing of PBO-BN/PVDF membrane. (**a**) Different pressure and cumulative intrusion curve of PBO-BN/PVDF separator. (**b**) The pore size distribution of PBO-BN/PVDF separator.

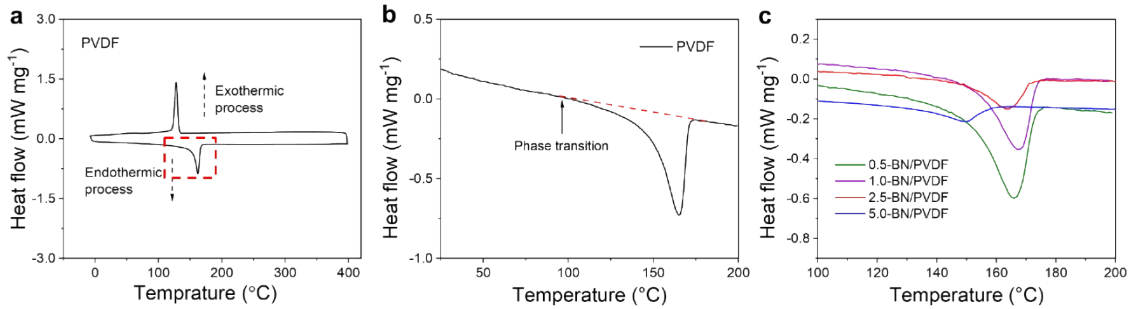

Supplementary Fig. 8 | Differential scanning calorimetry curves (DSC) of (**a**) PVDF membrane. Magnified DSC curves of (**b**) PVDF membrane and (**c**) *x*-BN/PVDF membrane (*x*-BN/PVDF, where *x* is the mass ratio of BN and PVDF). The DSC results reveal that the exothermic peak of PVDF is at 160 °C, but the phase transition of PVDF commences at approximately 100 °C. The DSC result of the BN/PVDF membrane reveals that the peak intensity of the exothermic peak decreases as the mass proportion of PVDF within BN/PVDF coating layer decreases. As a result, the low PVDF content of PBO-BN/PVDF resulted in DSC measurements falling below the sensitivity threshold of the instrumentation, which shows no discernible endothermic peak in 0–400 °C, similar to the DSC result of pure PBO membrane (Fig. 2b and Supplementary Fig. 2c).

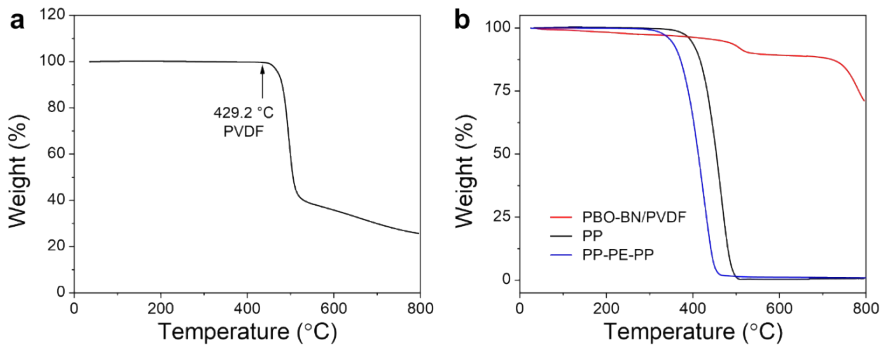

Supplementary Fig. 9 | Thermogravimetric analysis curves of (**a**) PVDF and (**b**) PP, PP-PE-PP, and PBO-BN/PVDF membranes. The PVDF membrane thermally deteriorates when exposed to temperatures above 429.2 °C, and the PBO membrane still exists superior thermal stability and remains intact until temperatures reach 670 °C.

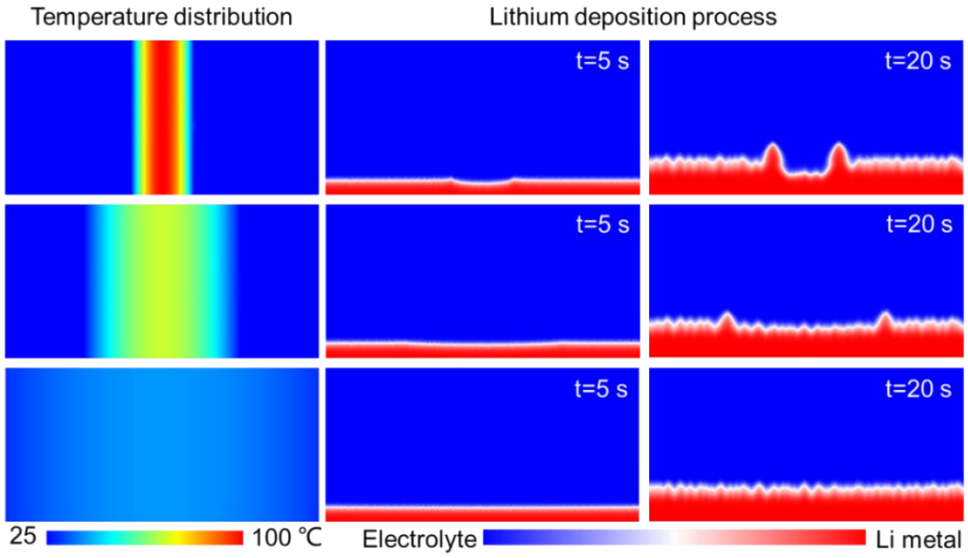

Supplementary Fig. 10 | The simulated Li deposition process on the Li metal surface (cross-sectional view) under different temperature distributions.

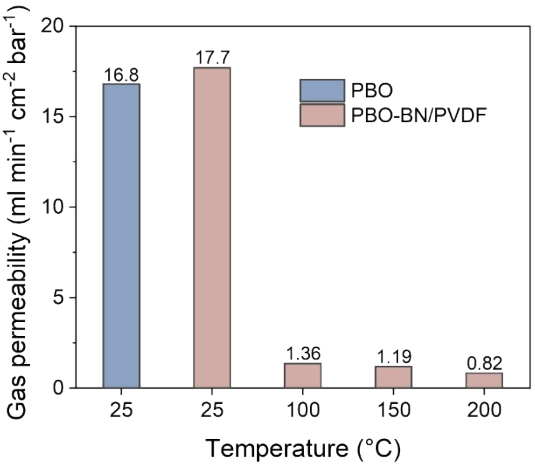

Supplementary Fig. 11 | Gas permeability of PBO at 25 °C and PBO-BN/PVDF separators at different temperatures. At a room temperature of 25 °C, PBO-BN/PVDF separator shows similar gas permeability to the PBO separator, indicating that the introduction of the BN/PVDF coating on the PBO membrane does not influence the gas permeability of the PBO matrix. Due to the overheating responding behavior of BN/PVDF coating layer, the gas permeability of PBO-BN/PVDF significantly decreases from 17.7 mL min^{-1} cm^{-2} bar^{-1} to 0.8 mL min^{-1} cm^{-2} bar^{-1} as the temperature experienced by the separator increases from 25 °C to 200 °C.

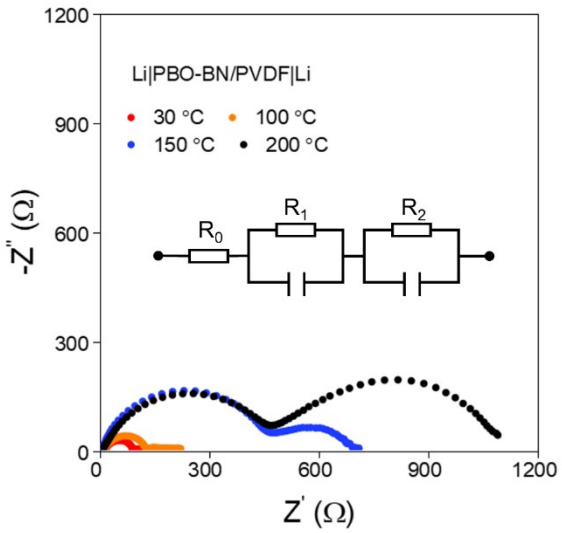

Supplementary Fig. 12 | Nyquist plots of the Li metal symmetric cell with the PBO-BN/PVDF separator under different temperatures. The real part impedance at the high-frequency end correlates with the ohmic impedance, which corresponds to the bulk impedance of the electrolyte (R_0). The real part impedance of the semicircle in the high-frequency and low-frequency regions correlates with the interface impedance between the BN/PVDF layer and the electrolyte (R_1) and the impedance of the solid-electrolyte interface(SEI, R_2), respectively. The ionic conductivity of electrolyte significantly decreases as the working temperature of the Li||Li symmetric cells with the PBO-BN/PVDF separators increases. These results indicate that once the internal temperature of the lithium batteries reaches to 150 °C, the heat-responsive coating layer of the PBO-BN/PVDF separators starts to block the pores and cut off ions transport between electrodes, and then to prevent further deterioration of thermal runaway.

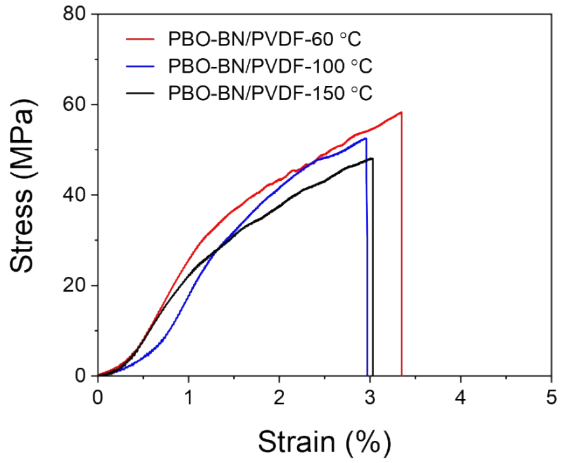

Supplementary Fig. 13 | Stress-strain curve of PBO-BN/PVDF separators under different temperatures. The tensile strength of PBO-BN/PVDF separator is 58.3 MPa at 60 °C, 52.5 MPa at 100 °C, and 48.1 MPa at 150 °C, which indicate that the PBO-BN/PVDF separator can still maintain excellent mechanical performance at elevated temperatures.

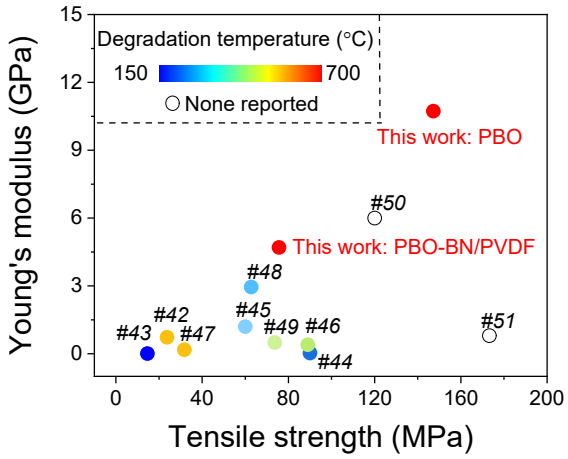

Supplementary Fig. 14 | Mechanical properties and degradation temperature of different separators.

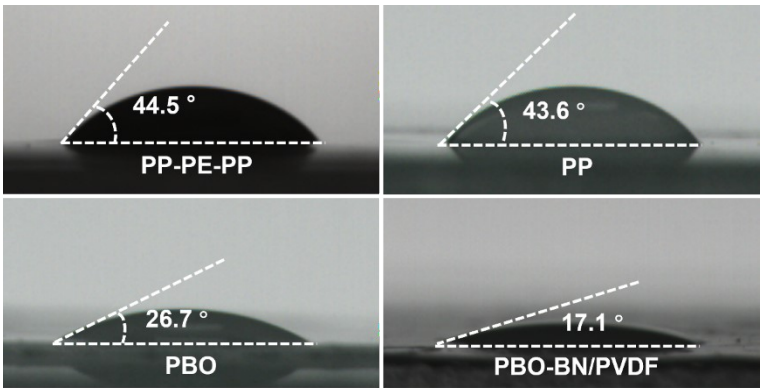

Supplementary Fig. 15 | The contact angle of liquid electrolytes on PP-PE-PP, PP, PBO, and PBO-BN/PVDF separators. The bare PBO membranes have lower contact angles with organic electrolyte compared to PP and PP-PE-PP separators (Fig. 2c), indicating that the PBO with the stronger organic affinity benefits electrolyte wettability and Li-ion transport. Benefiting from the enhanced interaction between the electrolyte and the polar functional groups of F and N in BN/PVDF layer, the PBO-BN/PVDF separator further improves the wettability of the electrolyte.

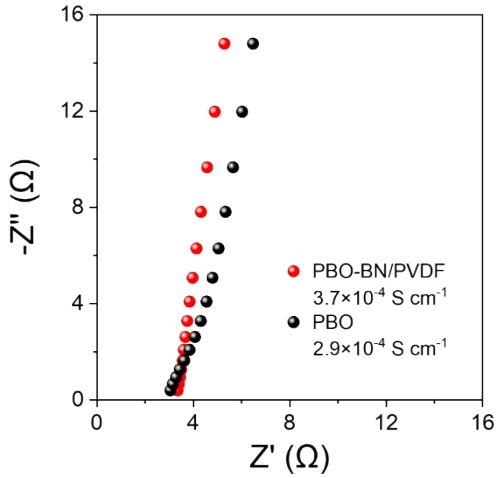

Supplementary Fig. 16 | Nyquist plots of SS|SS symmetric cells with PBO and PBO-BN/PVDF separators.

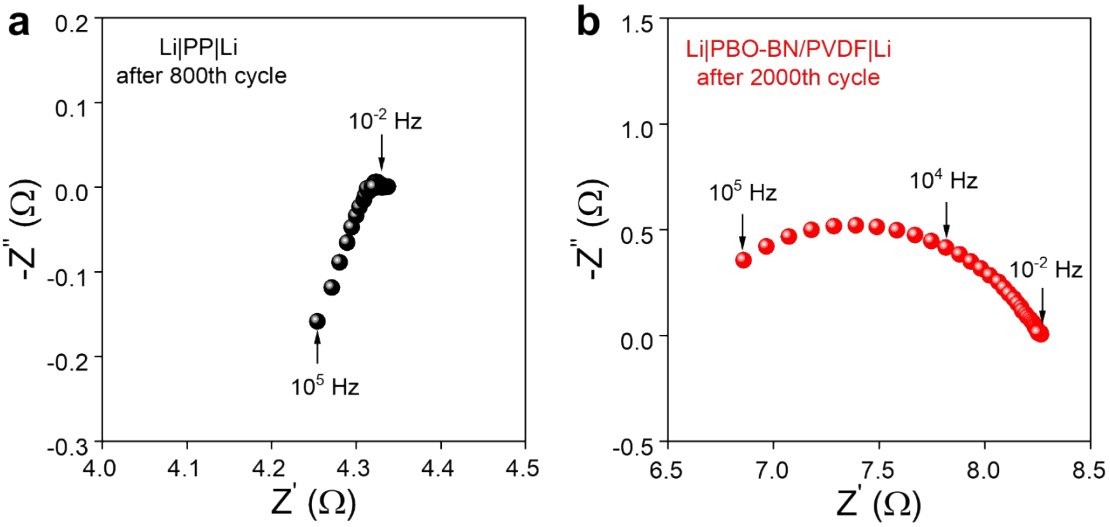

Supplementary Fig. 17 | Nyquist plots of Li|Li symmetric cells with (**a**) PP separators after cycling 800 h (**b**) PBO-BN/PVDF after cycling 2000 h. The EIS result of Li|PP|Li symmetric cell shows that the cell suffers internal short circuits after 800 h. In comparison, the Li|Li symmetric cells with PBO-BN/PVDF separators show low resistance without short circuit after cycling for 2000 h.

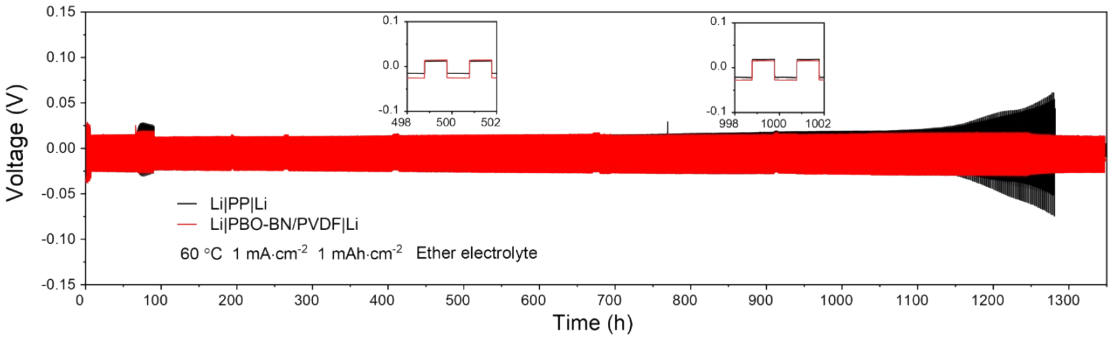

Supplementary Fig. 18 | Galvanostatic discharge/charge voltage profiles of the PBO-BN/PVDF and PP separators in Li|Li symmetric cells at 60 °C.

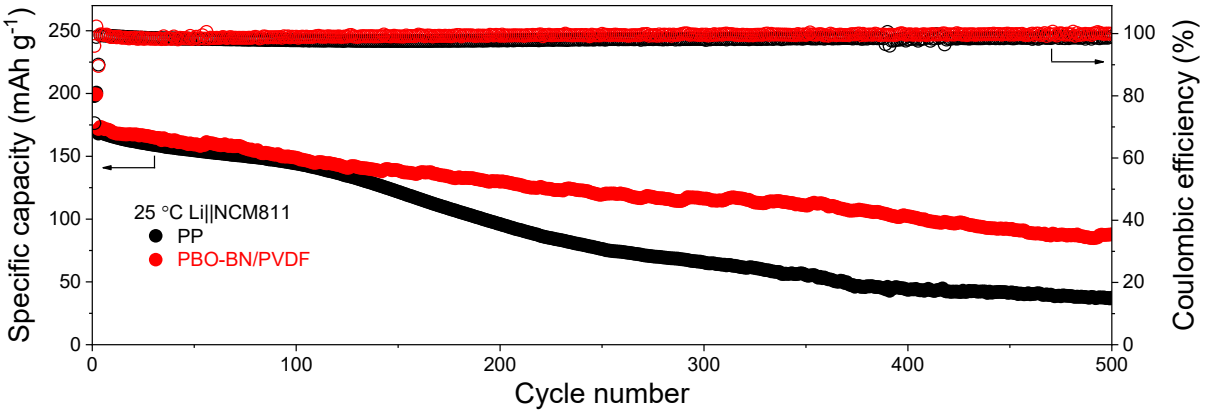

Supplementary Fig. 19 | Cycling performance of the Li|NCM811 cells at a current rate of 1.0 C with PP or PBO-BN/PVDF separators at 25 °C. These Li|NCM811 cells first cycled twice at 0.1 C rate to stabilize the anode and cathode interface and then cycled at a current density of 1.0 C rate (1.0 C=200 mA g^{-1}). At 25 °C, The Li|PBO-BN/PVDF|NCM811 cell has a specific capacity of 199.48 mAh g^{-1} in the first cycle at 0.1 C rate, and 171.73 mAh g^{-1} in the first cycle at 1.0 C rate, both slightly higher than those of the Li|PP|NCM811 cell (197.93 mAh g^{-1} at 0.1 C, 168.06 mAh g^{-1} at 1.0 C). After 500 cycles, the Li|PBO-BN/PVDF|NCM811 cell still retains a specific capacity of 87.92 mAh g^{-1} with a capacity retention of 51.20%, which is significantly better than that of the Li|PP|NCM811 cell with 37.46 mAh g^{-1} and 22.28%.

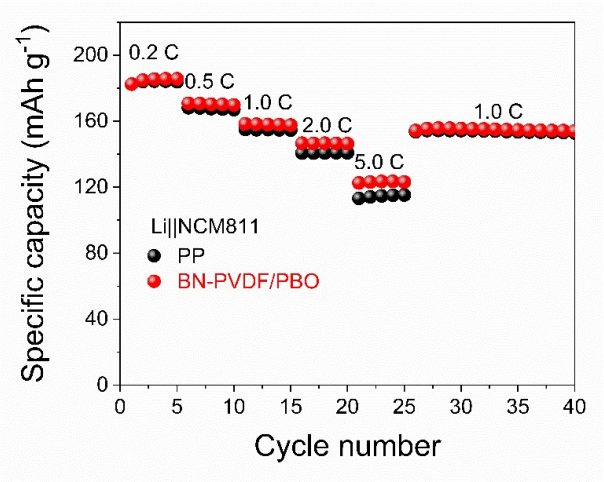

Supplementary Fig. 20 | Rate performance of the Li|NCM811 batteries with PP and PBO-BN/PVDF separators at 25 °C. The Li|PBO-BN/PVDF|NCM811 battery exhibits better rate performance than the Li|PP|NCM811 battery at 25 °C, which attributed to excellent electrolyte wettability of the PBO-BN/PVDF for the low charge transfer resistance.

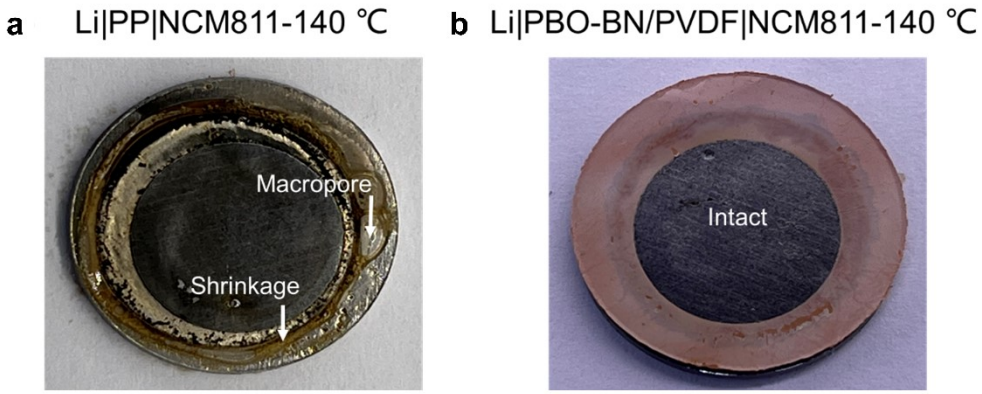

Supplementary Fig. 21 | Digital photo of PP and PBO-BN/PVDF separators in Li|NCM811 batteries after working at 140 °C. The PBO-BN/PVDF separators remain intact while the PP separators are badly damaged, indicating that the PBO-BN/PVDF separators can protect the safety of high-energy LMBs in overheating conditions.

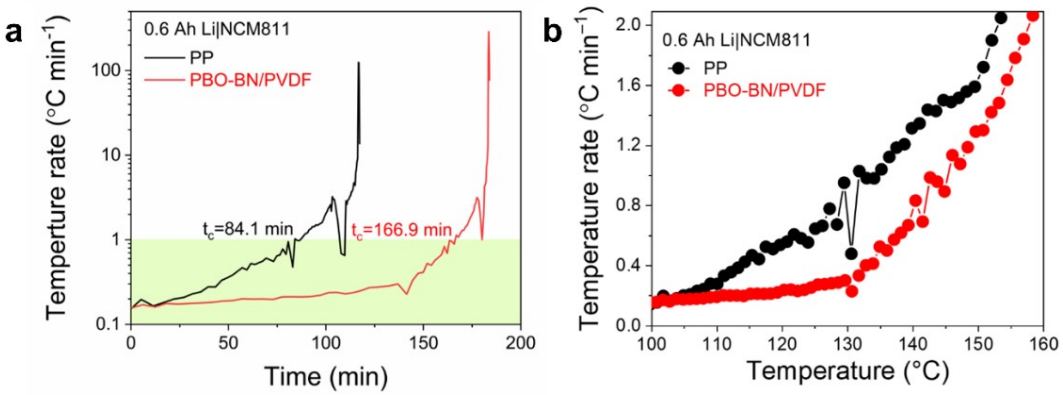

Supplementary Fig. 22 | Thermal runaway test result of 0.6 Ah Li|NCM811 pouch cells with PP and PBO-BN/PVDF separators. (**a**) Temperature rise rate with different time under thermal abusing conditions. (**b**) Temperature rise rate with different heating temperatures under thermal abusing conditions. The pouch cell with PBO-BN/PVDF separator always shows a lower temperature rise rate than that of the PP separator, indicating the PBO-BN/PVDF separator has a better ability for thermal management to prevent heat abuse from getting worse.

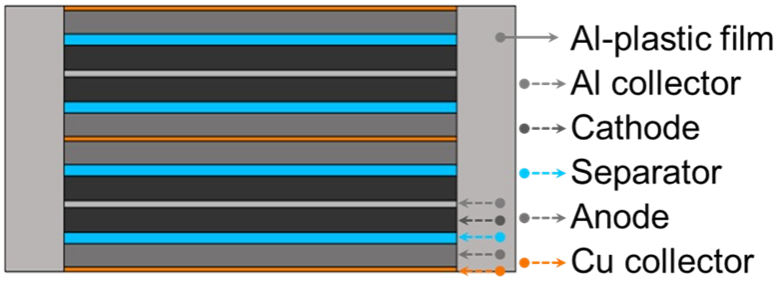

Supplementary Fig. 23 | The electro-chemo-thermal coupling model of pouch cell: The geometry for the pouch cell consists of multilayered Al collector|cathode|separator|anode|Cu collector units and Al-plastic films.

Supplementary Table 1 | Thermal conductivity of BN/PVDF membranes at different mass ratios.

Ratio of BN to PVDF	Temperature (°C)	Thermal conductivity (W m^{-1} K^{-1})
1.0-BN-PVDF	25	2.418
2.5-BN-PVDF	25	2.502
5.0-BN-PVDF	25	2.549

Supplementary Table 2 | The physical parameters of different commercial separators and PBO-BN/PVDF separator.

Separators	Porosity (%)	Thickness (μm)	Areal density(g m^{-2})
PP	55	25	11.1
PE	41	15	9.5
PP/PE/PP	39	20	10.9
PE-Al_2O_3	40	16	12.9
PBO-BN/PVDF	67.1	15.5	8.3

Supplementary Table 3 | Price comparison of raw materials for different commercial separators and PBO-BN/PVDF separator.

Separator	Unit cost of raw material ($ kg^{-1})
PP	1.5
PE	1.5
Cellulose	5
PBO	15
PVDF	25
PVDF-HFP	30

While the PBO-BN/PVDF separator demonstrates significant advancements in thermal safety, it is important to acknowledge that the current system does not yet offer a competitive price advantage. Future work will focus on refining the thermally stable materials used in the separator, aiming to strike a better balance between cost and performance.

Supplementary Table 4 | Mechanical parameters and degradation temperature of different separators.

Name	Tensile strength (MPa)	Young modulus (GPa)	Degradation temperature (°C)	Ref
PI	23.7	0.73	550	*(42)*
PVDF-HFP	14.6	0.01	169	*(43)*
PE-PVDF-HEC	90.0	0.03	420	*(44)*
Cellulose membrane	60.0	1.2	290	*(45)*
PI-PBI	89.0	0.40	540	*(46)*
FPI	31.7	0.18	550	*(47)*
Silk membrane	62.7	2.95	250	*(48)*
PI-SiO2	73.7	0.5	413	*(49)*
Cyanoethyl-chitin	120.0	6		*(50)*
PE	173.2	0.80		*(51)*
PBO-BN/PVDF	75.64	4.70	670	This work
PBO	147.22	10.73	670	This work

Supplementary Table 5 | Parameters used in the pseudo-three-dimensional model.

Specifications	**Cathode**	**Anode**	**Separator**
Thickness (m)	52.5×10^{-6}	50.0×10^{-6}	24.0×10^{-6}
Active particle radius (m)	4.3×10^{-6}	6.0×10^{-6}(C)	-
Max. Li-atom concentration (mol L^{-1})	49.79	31.37(C)	-
Initial electrolyte concentration (mol L^{-1})	1.0	1.0 (C)	1.0
The volume fraction of electrolyte	0.354	0.333(C)	0.432
Active material fraction	0.607	0.627(C)	-
Rate constant (m s^{-1})	2.0×10^{-11}	2.0×10^{-11}(C)	-
Cathode charge transfer coefficient	0.5	0.5	-
Anode charge transfer coefficient	0.5	0.5	-
Li-ion transference number	0.363	0.363(C)	0.363
The reference exchange current density (A m^{-2})		100 (Li)	

Note: The (C) parameter is only for carbon anode, and the (Li) parameter is only for Li metal anode.

Supplementary Table 6 | Parameters used in the energy conservation model.

Material	Density ($kg\ m^{-3}$)	Specific heat ($J\ kg^{-1}\ K^{-1}$)	Thermal conductivity ($W\ m^{-1}\ K^{-1}$)
Cathode	4870	840	1.58
Li metal anode	534	3580	84.8
C anode	2300	750	1
Electrolyte	1009	1978	0.334
Cu	8960	385	400
Al	2700	900	238
Al-plastic film	921	2300	3.6

Supplementary Table 7 | Parameters in the Li dendrite simulation part.

Symbol	Parameter	Value	unit
L_σ	Interfacial mobility	2.5×10^{-6}	$m^3\ J^{-1}\ s^{-1}$
L_η	Reaction constant	1.0	s^{-1}
κ	Gradient energy coefficient	5×10^{-5}	$J\ m^{-1}$
α	Cathodic charge-transfer coefficient	0.5	1
c_0	Li-ion concentration in bulk electrolyte	1.0	$mol\ L^{-1}$
c_s	Li atom concentration in metal solid	76.9	$mol\ L^{-1}$
D^e	Diffusion coefficient in electrode	7.5×10^{-13}	$m^2\ s^{-1}$
D^s	Diffusion coefficient in electrolyte	7.5×10^{-10}	$m^2\ s^{-1}$
σ^e	Conductivity in electrode	1.0×10^{7}	$S\ m^{-1}$
σ^s	Conductivity in electrolyte	1.0	$S\ m^{-1}$
T	Working temperature	298	K